

1 **SARS-CoV-2 infects lung epithelial cells and induces senescence and an inflammatory**
2 **response in patients with severe COVID-19**

3

4 Konstantinos Evangelou^{1*}, Dimitris Veroutis^{1*}, Periklis G. Foukas^{2*}, Koralia Paschalaki³,
5 Nefeli Lagopati¹, Marios Dimitriou⁴, Angelos Papaspyropoulos¹, Orsalia Hazapis¹,
6 Aikaterini Polyzou¹, Sophia Havaki¹, Athanassios Kotsinas¹, Christos Kittas¹, Athanasios G.
7 Tzioufas⁵, Laurence de Leval⁶, Demetris Vassilakos¹, Sotirios Tsiodras^{7,8}, Ioannis
8 Karakasiliotis⁴, Peter J Barnes^{3#} and Vassilis G. Gorgoulis^{1,9,10,11#}

9 1. Molecular Carcinogenesis Group, Department of Histology and Embryology,
10 Medical School, National and Kapodistrian University of Athens, Athens, Greece

11 2. 2nd Department of Pathology, Attikon University Hospital, Medical School, National
12 and Kapodistrian University of Athens, Athens, Greece

13 3. Airway Disease Section, National Heart and Lung Institute, Imperial College London,
14 London, UK

15 4. Laboratory of Biology, Department of Medicine, Democritus University of Thrace,
16 Alexandroupolis, Greece

17 5. Department of Pathophysiology, Medical School, National and Kapodistrian
18 University of Athens, Athens, Greece

19 6. Institute of Pathology, Lausanne University Hospital, Lausanne, Switzerland.

20 7. 4th Department of Internal Medicine, Attikon University Hospital, University of
21 Athens Medical School, Athens, Greece

22 8. Hellenic Centre for Disease Control and Prevention, Athens, Greece.

23 9. Faculty Institute for Cancer Sciences, Manchester Academic Health Sciences Centre,
24 University of Manchester, Manchester, UK

25 10. Biomedical Research Foundation, Academy of Athens, Athens, Greece

26 11. Center for New Biotechnologies and Precision Medicine, Medical School, National
27 and Kapodistrian University of Athens, Athens, Greece

28

29 ***equally contributed**

30

31 Key words: SARS-Cov-2, monoclonal antibody, COVID-19, cellular senescence,
32 senescence-associated secretory phenotype (SASP), angiotensin-converting-enzyme 2
33 (ACE2), alveolar type-2 (AT2) cells, DNA damage, SenTraGor

34

35

36 **Short title:** SARS-Cov-2 infected human alveolar cells exhibit features of cellular
37 senescence

38 **# Corresponding Authors:** Peter J Barnes, p.j.barnes@imperial.ac.uk

39 Vassilis G Gorgoulis, vgorg@med.uoa.gr

40

41

42 **Abstract**

43

44 **Rationale:** SARS-CoV-2 infection of the respiratory system can progress to a life
45 threatening multi-systemic disease, mediated via an excess of cytokines ("cytokine
46 storm"), but the molecular mechanisms are poorly understood.

47 **Objectives:** To investigate whether SARS-CoV-2 may induce cellular senescence in lung
48 epithelial cells, leading to secretion of inflammatory cytokines, known as the senescence-
49 associated secretory phenotype (SASP).

50 **Methods:** Autopsy lung tissue samples from eleven COVID-19 patients and sixty age-
51 matched non-infected controls were analysed by immunohistochemistry for SARS-CoV-2
52 and markers of cellular senescence (SenTraGor, p16^{INK4A}) and key SASP cytokines
53 (interleukin-1 β , interleukin-6). We also investigated whether SARS-CoV-2 infection of an
54 epithelial cell line induces senescence and cytokine secretion.

55 **Measurements and Main Results:** SARS-CoV-2 was detected by immunocytochemistry
56 and electron microscopy predominantly in alveolar type-2 (AT2) cells, which also
57 expressed the angiotensin-converting-enzyme 2 (ACE2), a critical entry receptor for this
58 virus. In COVID-19 samples, AT2 cells displayed increased markers of senescence
59 [p16^{INK4A}, SenTraGor staining positivity in 12 \pm 1.2% of cells compared to 1.7 \pm 0.13% in non-
60 infected controls (p <0.001)], with markedly increased expression of interleukin-1 β and
61 interleukin-6 (p <0.001). Infection of epithelial cells (Vero E6) with SARS-CoV-2 *in-vitro*
62 induced senescence and DNA damage (increased SenTraGor and γ -H2AX), and reduced
63 proliferation (Ki67) compared to uninfected control cells (p <0.01).

64 **Conclusions:** We demonstrate that in severe COVID-19 patients, AT2 cells are infected
65 with SARS-CoV-2 and show senescence and expression of proinflammatory cytokines. We
66 also show that SARS-CoV-2 infection of epithelial cells may induce senescence and
67 inflammation, indicating that cellular senescence may be an important molecular
68 mechanism of severe COVID-19.

69

70

71 **Introduction**

72 The severe acute respiratory syndrome coronavirus 2 (SARS-CoV-2) causes the
73 Coronavirus disease 2019 (COVID-19) that primarily affects the respiratory system. The
74 clinical course of the patients ranges from asymptomatic to a life-threatening respiratory
75 failure accompanied by a multi-systemic inflammatory disease (1,2). Systemic disease
76 may occur through a viral-mediated "cytokine storm" that consists of a variety of
77 cytokines and chemokines (CXCL-10, CCL-2, IL-6, IL-8, IL-12, IL1 β , IFN- γ , TNF- α) (3,4). The
78 link between viral infection of cells and development of severe lung disease and systemic
79 manifestations is still poorly understood. Viral infection results in the activation of
80 complex innate and adaptive immune responses that are orchestrated sequentially,
81 involving several cell types and inflammatory mediators (5,6). At the cellular level,
82 intrinsic defence mechanisms are activated and outcomes range from complete recovery
83 to cell death (7-11). An "intermediate" and essential cellular state that is overlooked, due
84 to lack of efficient methodological tools, is cellular senescence (12,13).

85 Cellular senescence is a stress response mechanism that preserves organismal
86 homeostasis. Senescent cells are characterized by prolonged and generally irreversible
87 cell-cycle arrest and resistance to apoptosis (12,14). Additionally, they also exhibit
88 secretory features collectively described, as the senescence-associated secretory
89 phenotype (SASP) (12). SASP includes a variety of cytokines, chemokines, growth factors,
90 proteases and other molecules, depending on the senescence type (12,15). They are
91 released in the extracellular space as soluble factors, transmembrane proteins following
92 ectodomain shedding, or as molecules engulfed within small exosome-like vesicles (16-
93 18). Under physiological conditions, senescence is transiently activated and SASP

94 mediates the recruitment of immune cells for senescent cell clearance. In addition, other
95 SASP factors promote tissue regeneration and repair, overall ensuring cellular/tissue
96 homeostasis. On the contrary, persistence of senescent cells exerts harmful properties
97 promoting tissue dysfunction and the maintenance of a “latent” chronic inflammatory
98 milieu, via paracrine and systemic SASP (12,15).

99 There is little published evidence linking viral infection to cellular senescence (19-22).
100 Given the significance of the “cytokine storm” in the progression of COVID-19 and the
101 SASP secretion by senescent cells, we investigated whether cellular senescence occurs in
102 COVID-19. We provide the first evidence supporting not only the evidence for senescence
103 in COVID-19 infected lung cells, but also potential long-term adverse implications of this
104 disease process.

105

106 **Materials and Methods**

107

108 **Lung tissue**

109 Formalin Fixed and Paraffin embedded autopsy lung tissue samples from eleven patients
110 that died from COVID-19 (confirmed by RT-qPCR) and lung tissues resected prior to the
111 COVID-19 outbreak, comprising a cohort of sixty previously published and new cases
112 (negative controls) were analyzed (**Suppl. Table 1**) (23). Clinical sample collection and
113 their experimental use were approved by the Commission Cantonale D'éthique de la
114 Recherche, University of Lausanne, Switzerland (Ref 2020-01257), the Bio-Ethics
115 Committee of University of Athens Medical School, Greece.

116

117 **Anti-SARS-COV-2 (G2) antibody generation**

118 Mice immunization and antibodies collection, selection and specificity determination are
119 described in detail in **Suppl Information**. Transcriptome analysis of hybridomas and
120 amino acid determination of selected clones are also provided in **Suppl Information**. Four
121 clones, namely 479-S1, 480-S2, 481-S3 and 482-S4 are under patent application
122 (**Gorgoulis V.G., Vassilakos D. and Kastrinakis N. (2020) GR-patent application no: 22-**
123 **0003846810**).

124

125 **Cells and SARS-CoV-2 culture**

126 SARS-CoV-2 [isolate 30-287 (B.1.222 strain)] was obtained through culture in Vero E6
127 cells (ATCC® CRL-1586), from an infected patient in Greece. The virus was recovered from
128 a nasopharyngeal swab, rinsed in 1 ml saline and filtered twice through a 0.22 µm filter.

129 Virus stock was prepared by infecting fully confluent Vero E6 cells in DMEM, 10% fetal
130 bovine serum (FBS), with antibiotics, at 37°C, 5% CO₂. Virus stock was collected four days
131 after inoculation, sequenced by NGS (**Suppl Information**) and the supernatant was frozen
132 (-80°C) until use. Infections were carried out in 24-well plates, using SARS-CoV-2 at a 0.01
133 MOI. Cells were either fixed with 4% paraformaldehyde or lysed with NucleoZOL
134 (MACHEREY-NAGEL) 17 days post infection. Manipulations were carried out in a Biosafety
135 level 3 facility.

136

137 **RNA extraction and Reverse-Transcription real-time PCR (RT-qPCR)** detection were
138 performed as previously described (**Suppl Information**) (24).

139

140 **Next Generation Sequencing (NGS)**

141 NGS was performed as previously described (25). Briefly, the Ion AmpliSeq Library Kit
142 Plus was used to generate libraries following the manufacturer's instruction, employing
143 the Ion AmpliSeq SARS-CoV-2 RNA custom primers panel (ID: 05280253, Thermo Fisher
144 Scientific). Briefly, library preparation steps involved reverse transcription of RNA using
145 the SuperScript VILO cDNA synthesis kit (Thermo Fisher Scientific), 17-19 cycles of PCR
146 amplification, adapter ligation, library purification using the Agencourt_AMPure XP
147 (Beckman Coulter), and library quantification using Qubit Fluorometer high-sensitivity kit.
148 Ion 530 Chips were prepared using Ion Chef and NGS reactions were run on an Ion
149 GeneStudio S5, ion torrent sequencer (Thermo Fisher Scientific). Samples were run in
150 triplicates.

151

152 **Immunocytochemistry and Immunohistochemistry**

153 ICC and IHC were performed according to published protocols (26). The following primary
154 antibodies were applied overnight at 4°C: i) anti-SARS-CoV-2 (G2) monoclonal antibody
155 (at a dilution 1:300), ii) anti-ACE-2 (Abcam), iii) anti- TTF-1 (Dako), iv) anti-CD68 (Dako)
156 and v) anti-p16^{INK4A} (Santa Cruz), vi) anti-IL-1 β (Abcam) and vii) anti-IL-6 (R&D systems),
157 viii) anti- phospho-histone (Ser 139) 2AX (γ H2AX) (Cell Signaling) and ix) anti-Ki67
158 (Abcam)(Suppl Information).

159

160 **SenTraGor™ staining and double staining** experiments were performed and evaluated
161 as previously described (26).

162

163 **Electron Microscopy**

164 Representative area from hematoxylin and eosin stained paraffin sections of the lung
165 autopsy of COVID-19 patients and corresponding non COVID-19 controls were chosen
166 under the light microscope and marked. Paraffin-embedded tissue was deparaffinized,
167 rehydrated and fixed in 2.5% glutaraldehyde in PBS for 24h and post-fixed in 1% aqueous
168 osmium tetroxide for 1h at 4°C. The tissue fragment was embedded in fresh epoxy resin
169 mixture, stained with ethanolic uranyl acetate and lead citrate and observed with a FEI
170 Morgagni 268 transmission electron microscope equipped with Olympus Morada digital
171 camera.

172

173 **Statistical analysis**

174 The Wilcoxon paired non-parametric test was used to compare GL13 labelling indices and
175 levels of IL-6, IL-8 and IL-1 β between two groups (non-COVID-19 and COVID-19 infected).
176

177 **Results**

178

179 **Detection of SARS-CoV-2 in lung cells**

180 In order to detect SARS-CoV2 in lung tissue we developed monoclonal antibodies which
181 react against the spike protein of SARS-CoV-2 and identified a high affinity antibody (G2)
182 (**Suppl Figure 1, Suppl Figure 2, Suppl. Table 1A and Suppl. Table 1B**) (23). SARS-CoV-2
183 was detected predominantly in alveolar type 2 (AT2) cells, which are identified by TTF-1
184 positivity, and in sparse inflammatory cells (alveolar and tissue macrophages) in all
185 COVID-19 patients (**Figure 1A, C**), ranging from <5 cells/4mm² tissue to >50 cells/4mm²
186 tissue (**Suppl. Table 1A**). SARS-CoV-2 infected AT2 cells were occasionally large and
187 appeared isolated (denuded or syncytial) or clustered (hyperplasia), exhibiting a variety
188 of topological distribution (**Figure 1A**). These cells co-expressed the angiotensin-
189 converting enzyme 2 (ACE2) receptor (**Figure 1B**), supporting SARS-Cov-2 infection being
190 mediated by the ACE2 receptor (27). In addition, electron microscopy analysis in
191 representative COVID-19 cases confirmed the presence of virus within AT2 cells (**Figure**
192 **1Ci,ii**) and high magnification revealed virions in the proximity of the endoplasmic
193 reticulum (**Figure 1Ciii,iv**) indicating their likely assembly and budding, as well as virions
194 residing in cytoplasmic vesicles (**Figure 1Ciii,v-vi**), implying their transfer and release into
195 the extracellular space.

196

197 **Senescence in SARS-CoV-2 infected cells**

198 A proportion of SARS-CoV-2 infected AT2 cells (range 8 to 21%) displayed a senescent
199 phenotype, with positive staining for SenTraGor and p16^{INK4A} (**Figure 2A-C**) (12,26-28). By

200 contrast lung tissues from age-matched non-COVID-19 cases with analogous co-
201 morbidities (**Suppl Table 1**) showed significantly lower senescence (range 1-2%, $p < 0.01$,
202 Wilcoxon paired non-parametric test) (**Figure 2A-C**), suggesting that SARS-CoV-2 infection
203 may induce senescence.

204 To functionally reproduce our hypothesis we infected Vero cells with a viral strain
205 isolated from a COVID-19 patient. Vero cells is an established cellular system for viral
206 propagation and studies, as apart from their high infectivity to SARS-CoV-2 they are
207 among the few cell lines demonstrating SARS-CoV-2-mediated cytopathic effects, an
208 essential aspect in diagnostics (29,30). Infection was carried out at a low MOI to mimic
209 natural coronavirus infection (31). In line with our hypothesis, the infected cells following
210 an initial surge of cell death reached an equilibrium demonstrating clear evidence of
211 senescence, as compared to the non-infected control cells, 17 days post infection (**Figure**
212 **3**). As Vero cells lack p16^{INK4A} (32), the most likely trigger of senescence is DNA damage,
213 as previously reported (12,33). DNA damage measured by γ -H2AX immunostaining, was
214 evident in SARS-CoV-2 infected cells (**Figure 3A4**). It appears that genotoxic stress results
215 from a vicious cycle imposed by the virus in host cells as it hijacks most intracellular
216 protein machineries (11,34).

217

218 **Senescence associated secretory phenotype**

219 We found very high expression of both IL-1 β and IL-6 by senescent AT2 cells in the lungs
220 of COVID-19 patients while in the non COVID-19 control cases expression was very low in
221 the few senescent AT2 cells detected ($p < 0.001$) (**Figure 4A-C, Suppl Table 1**). As both
222 cytokines are key components of the "cytokine storm", our findings suggest putative

223 implication of senescence via SASP in the poor clinical course of COVID-19 patients.

224 Likewise, SARS-CoV-2 senescent Vero cells displayed expression of SASP-related

225 cytokines, as assessed by our recently reported algorithmic assessment of senescence,

226 justifying the *in vivo* findings (**Figure 3B**).

227

228

229 **Discussion**

230 We have demonstrated the presence of SARS-CoV-2 in AT2 cells of patients who died
231 from COVID-19 using a novel anti-viral antibody and confirmed by electron microscopy.
232 We have shown for the first time that a proportion of SARS-CoV-2-infected AT2 cells
233 acquire senescence features (as demonstrated by significantly increased staining with the
234 novel senescence marker SenTraGor and increased p16^{INK4A}). The finding that in age-
235 matched non-COVID-19 cases the percentage of senescent cells was much lower (1-2%)
236 than that of the COVID-19 clinical panel (8-21%), is strongly indicative that SARS-CoV-2
237 triggers senescence (**Figure 2**). We therefore examined whether cellular infection with
238 SARS-CoV-2 virus (B.1.222 strain) would induce cellular senescence in a susceptible cell
239 line *in vitro* and found that in infected cells there was increased SenTraGor staining, as
240 well as evidence of DNA damage measured by increased γ -H2AX expression. This strongly
241 suggests that SARS-CoV-2 may attach to AT2 cells via ACE2 to infect these cells and
242 through activation of the DNA damage response may induce cellular senescence (34). We
243 also demonstrated that the cells infected with SARS-CoV-2 also show a high degree of
244 expression of IL-1 β and IL-6, both components of the SASP and implicated in systemic
245 features of COVID-19 which is associated with a “cytokine storm” (3,4).

246 Senescent cells are in a state of cell cycle arrest but remain metabolically active and
247 secrete a typical profile of inflammatory proteins known as the senescence-associated
248 secretory phenotype (SASP). SASP components include the proinflammatory cytokines IL-
249 1 β and IL-6, which are elevated in COVID-19 patients that have acute respiratory distress
250 syndrome (ARDS) or systemic inflammatory features. The SASP components could induce
251 senescence in nearby cells (paracrine) or may spread senescence systemically

252 (endocrine), thus amplifying this chronic inflammation. It is likely that SARS-CoV-2
253 spreads from epithelial cells in the lower airways to infect AT2 cells, which express ACE2,
254 and cause local senescence and inflammation in the lung. The virus may then enter the
255 circulation and senescence may subsequently spread systemically to affect other organs,
256 leading to multi-organ failure and death (1,22)

257 An additional implication relates to the prolonged survival of senescent cells that are
258 infected with the virus, as senescent cells are resistant to apoptosis (12,14). This may
259 allow the virus to be hosted for longer periods compared to other cells with higher cell
260 turnover, exposing its genome to host-mediated editing (35-38). Within this context, we
261 recently reported abundance of the APOBEC enzymes, particularly G and H (RNA editing
262 cytoplasmic variants), which are reported to play a pivotal role in viral RNA editing, in
263 cells undergoing stress-induced senescence (24,39,40). In support to this notion, are the
264 increased APOBEC 3G and 3H expression levels found in the infected Vero cells (**Suppl**
265 **Figure 3**). Moreover, by conducting a detailed bioinformatic analysis of 423000 SARS-
266 CoV-2 strains available in the GISAID database, we found that APOBEC signatures seem to
267 potently determine the mutational profile of the SARS-CoV-2 genome (**Suppl Figure 4,**
268 **Suppl Figure 5**).

269 A limitation of the study is the small sample size of examined COVID-19 lung autopsies,
270 due to difficulty of getting access to this material. Another limitation due to the nature of
271 the disease is that pathological features, such as senescence, can only be investigated
272 within the context of cadaverous material, which represents the most severe outcome of
273 the spectrum of COVID-19 clinical manifestations. Therefore, evaluation of senescence in

274 less severe conditions is not feasible. Findings have been observed in lung biopsies only
275 and ideally should be also investigated in organs other than the lung.

276 Overall, SARS-CoV-2 induced senescence justifies the application of senotherapeutics
277 not only as a therapeutic approach for the treatment of COVID-19 patients but also as a
278 putative strategy to restrict mutational events that may favor the emergence of SARS-
279 CoV-2 quasispecies (15,22,41). Senotherapies include senostatics that inhibit components
280 of the cellular senescence pathways and senolytics, which induce senescent cells to
281 become apoptotic (15,22). Several senolytic therapies have been shown to be effective in
282 animal models of accelerated ageing diseases, including COPD, idiopathic pulmonary
283 fibrosis, atherosclerosis and chronic kidney disease (12,15,22). A trial of senolytic therapy
284 in patients with diabetic kidney disease demonstrated a reduction in senescent cells in
285 the skin and reduced circulating SASP proteins, such as IL-1 β and IL-6 (42). A clinical trial
286 of a Senolytic compound (F) to inhibit progression to cytokine storm and ARDS in COVID-
287 19 patients has been approved by the US Food and Drug Administration (FDA) and is
288 anticipated to be soon launched (43).

289

290

291 **Disclosure/Conflict of Interest**

292 The authors wish to declare no conflict of interest.

293

294 **Acknowledgements:**

295 We would like to thank Konstantinos Ntostoglou for his valuable help in preparing the
296 material. We acknowledge support in RNA sequencing by the “The Greek Research

297 Infrastructure for Personalised Medicine (pMED-GR)" (MIS 5002802) which is
298 implemented under the Action "Reinforcement of the Research and Innovation
299 Infrastructure", funded by the Operational Programme "Competitiveness,
300 Entrepreneurship and Innovation" (NSRF 2014-2020) and co-financed by Greece and the
301 European Union (European Regional Development Fund). This work was supported by
302 the: National Public Investment Program of the Ministry of Development and Investment
303 / General Secretariat for Research and Technology, in the framework of the Flagship
304 Initiative to address SARS-CoV-2 (2020ΣΕ01300001); Horizon 2020 Marie Skłodowska-
305 Curie training program no. 722729 (SYNTRAIN); Welfare Foundation for Social & Cultural
306 Sciences, Athens, Greece (KIKPE); H. Pappas donation; Hellenic Foundation for Research
307 and Innovation (HFRI) grants no. 775 and 3782 and NKUA-SARG grant 70/3/8916.

308

309

310 **References**

- 311 1. Hu B, Guo H, Zhou P, Shi ZL. Characteristics of SARS-CoV-2 and COVID-19. *Nat Rev*
312 *Microbiol* 2021; 19: 141–154.
- 313 2. Robba C, Battaglini D, Ball L, Patroniti N, Loconte M, Brunetti I, Vena A, Giacobbe
314 DR, Bassetti M, Rocco PRM, Pelosi P. Distinct phenotypes require distinct respiratory
315 management strategies in severe COVID-19. *Respir Physiol Neurobiol* 2020; 279: 103455.
- 316 3. Del Valle DM, Kim-Schulze S, Huang HH, Beckmann ND, Nirenberg S, Wang B, Lavin
317 Y, Swartz TH, Madduri D, Stock A, Marron TU, Xie H, Patel M, Tuballes K, Van Oekelen O,
318 Rahman A, Kovatch P, Aberg JA, Schadt E, Jagannath S, Mazumdar M, Charney AW, Firpo-
319 Betancourt A, Mendu DR, Jhang J, Reich D, Sigel K, Cordon-Cardo C, Feldmann M, Parekh
320 S, Merad M, Gnjjatic S. An inflammatory cytokine signature predicts COVID-19 severity
321 and survival. *Nat Med* 2020; 26: 1636–1643.
- 322 4. Tang Y, Liu J, Zhang D, Xu Z, Ji J, Wen C. Cytokine Storm in COVID-19: The Current
323 Evidence and Treatment Strategies. *Front Immunol* 2020; 11: 1708.
- 324 5. Poland GA, Ovsyannikova IG, Kennedy RB. SARS-CoV-2 immunity: review and
325 applications to phase 3 vaccine candidates. *Lancet* 2020; 396: 1595–1606.
- 326 6. Zhang F, Gan R, Zhen Z, Hu X, Li X, Zhou F, Liu Y, Chen C, Xie S, Zhang B, Wu X,
327 Huang Z. Adaptive immune responses to SARS-CoV-2 infection in severe versus mild
328 individuals. *Signal Transduct Target Ther* 2020; 5: 156.
- 329 7. Rouse BT, Sehrawat S. Immunity and immunopathology to viruses: what decides
330 the outcome? *Nat Rev Immunol* 2010; 10: 514–526.
- 331 8. Mocarski ES, Upton JW, Kaiser WJ. Viral infection and the evolution of caspase 8-
332 regulated apoptotic and necrotic death pathways. *Nat Rev Immunol* 2011; 12: 79–88.

- 333 9. Braciale TJ, Sun J, Kim TS. Regulating the adaptive immune response to respiratory
334 virus infection. *Nat Rev Immunol* 2012; 12: 295–305.
- 335 10. Fan Y, Sanyal S, Bruzzone R. Breaking Bad: How Viruses Subvert the Cell Cycle. *Front*
336 *Cell Infect Microbiol* 2018; 8: 396.
- 337 11. Hekman RM, Hume AJ, Goel RK, Abo KM, Huang J, Blum BC, Werder RB, Suder EL,
338 Paul I, Phanse S, Youssef A, Alysandratos KD, Padhorny D, Ojha S, Mora-Martin A, Kretov
339 D, Ash PEA, Verma M, Zhao J, Patten JJ, Villacorta-Martin C, Bolzan D, Perea-Resa C,
340 Bullitt E, Hinds A, Tilston-Lunel A, Varelas X, Farhangmehr S, Braunschweig U, Kwan JH,
341 McComb M, Basu A, Saeed M, Perissi V, Burks EJ, Layne MD, Connor JH, Davey R, Cheng
342 JX, Wolozin BL, Blencowe BJ, Wuchty S, Lyons SM, Kozakov D, Cifuentes D, Blower M,
343 Kotton DN, Wilson AA, Mühlberger E, Emili A. Actionable Cytopathogenic Host
344 Responses of Human Alveolar Type 2 Cells to SARS-CoV-2. *Mol Cell* 2021; 81: 212.
- 345 12. Gorgoulis V, Adams PD, Alimonti A, Bennett DC, Bischof O, Bishop C, Campisi J,
346 Collado M, Evangelou K, Ferbeyre G, Gil J, Hara E, Krizhanovsky V, Jurk D, Maier AB,
347 Narita M, Niedernhofer L, Passos JF, Robbins PD, Schmitt CA, Sedivy J, Vougas K, von
348 Zglinicki T, Zhou D, Serrano M, Demaria M. Cellular Senescence: Defining a Path Forward.
349 *Cell* 2019; 179: 813–827.
- 350 13. Rendeiro AF, Ravichandran H, Bram Y, Salvatore S, Borczuk A, Elemento O,
351 Schwartz RE. The spatio-temporal landscape of lung pathology in SARS-CoV-2 infection.
352 medRxiv: the preprint server for health sciences, 2020.10.26.20219584.
- 353 14. Childs BG, Baker DJ, Kirkland JL, Campisi J, van Deursen JM. Senescence and
354 apoptosis: dueling or complementary cell fates? *EMBO Rep* 2014; 15: 1139–1153.

- 355 15. Myrianthopoulos V, Evangelou K, Vasileiou PVS, Cooks T, Vassilakopoulos TP,
356 Pangalis GA, Kouloukoussa M, Kittas C, Georgakilas AG, Gorgoulis VG. Senescence and
357 senotherapeutics: a new field in cancer therapy. *Pharmacol Ther* 2019; 193: 31–49.
- 358 16. Özcan S, Alessio N, Acar MB, Mert E, Omerli F, Peluso G, Galderisi U. Unbiased
359 analysis of senescence associated secretory phenotype (SASP) to identify common
360 components following different genotoxic stresses. *Aging* 2016; 8: 1316–1329.
- 361 17. Basisty N, Kale A, Jeon OH, Kuehnemann C, Payne T, Rao C, Holtz A, Shah S, Sharma
362 V, Ferrucci L, Campisi J, Schilling B. A proteomic atlas of senescence-associated
363 secretomes for aging biomarker development. *PLoS Biol* 2020; 18: e3000599.
- 364 18. Faget DV, Ren Q, Stewart SA. Unmasking senescence: context-dependent effects of
365 SASP in cancer. *Nat Rev Cancer* 2019; 19: 439–453.
- 366 19. Baz-Martínez M, Da Silva-Álvarez S, Rodríguez E, Guerra J, El Motiam A, Vidal A,
367 García-Caballero T, González-Barcia M, Sánchez L, Muñoz-Fontela C, Collado M, Rivas C.
368 Cell senescence is an antiviral defense mechanism. *Sci Rep* 2016; 6: 37007.
- 369 20. Chuprin A, Gal H, Biron-Shental T, Biran A, Amiel A, Rozenblatt S, Krizhanovsky V.
370 Cell fusion induced by ERVWE1 or measles virus causes cellular senescence. *Genes Dev*
371 2013; 27: 2356–2366.
- 372 21. Kelley WJ, Zemans RL, Goldstein DR. Cellular senescence: friend or foe to
373 respiratory viral infections? *Eur Respir J* 2020; 56: 2002708.
- 374 22. Kohli J, Veenstra I, Demaria M. The struggle of a good friend getting old: cellular
375 senescence in viral responses and therapy. *EMBO Rep* 2021; 22: e52243.
- 376 23. Gorgoulis VG, Vassiliou LV, Karakaidos P, Zacharatos P, Kotsinas A, Liloglou T,
377 Venere M, Ditullio RA Jr, Kastrinakis NG, Levy B, Kletsas D, Yoneta A, Herlyn M, Kittas C,

- 378 Halazonetis TD. Activation of the DNA damage checkpoint and genomic instability in
379 human precancerous lesions. *Nature* 2005; 434: 907–913.
- 380 24. Komseli ES, Pateras IS, Krejsgaard T, Stawiski K, Rizou SV, Polyzos A, Roumelioti FM,
381 Chiourea M, Mourkioti I, Paparouna E, Zampetidis CP, Gumeni S, Trougakos IP, Pefani DE,
382 O'Neill E, Gagos S, Eliopoulos AG, Fendler W, Chowdhury D, Bartek J, Gorgoulis VG. A
383 prototypical non-malignant epithelial model to study genome dynamics and concurrently
384 monitor micro-RNAs and proteins in situ during oncogene-induced senescence. *BMC*
385 *Genomics* 2018; 19: 37.
- 386 25. Lagopati N, Tsioli P, Mourkioti I, Polyzou A, Papaspyropoulos A, Zafiropoulos A,
387 Evangelou K, Sourvinos G, Gorgoulis VG. Sample pooling strategies for SARS-CoV-2
388 detection. *J Virol Methods* 2021; 289: 114044.
- 389 26. Evangelou K, Lougiakis N, Rizou SV, Kotsinas A, Kletsas D, Muñoz-Espín D,
390 Kastrinakis NG, Pouli N, Marakos P, Townsend P, Serrano M, Bartek J, Gorgoulis VG.
391 Robust, universal biomarker assay to detect senescent cells in biological specimens.
392 *Aging Cell* 2017; 16: 192–197.
- 393 27. Wang Q, Zhang Y, Wu L, Niu S, Song C, Zhang Z, Lu G, Qiao C, Hu Y, Yuen KY, Wang
394 Q, Zhou H, Yan J, Qi J. Structural and Functional Basis of SARS-CoV-2 Entry by Using
395 Human ACE2. *Cell* 2020; 181: 894–904.e9.
- 396 28. Kohli J, Wang B, Brandenburg SM, Basisty N, Evangelou K, Varela-Eirin M, Campisi J,
397 Schilling B, Gorgoulis V, Demaria M. Algorithmic assessment of cellular senescence in
398 experimental and clinical specimens. *Nat Protoc* 2021; 10.1038/s41596-021-00505-5.
399 Advance online publication.

- 400 29. Wurtz N, Penant G, Jardot P, Duclos N, La Scola B. Culture of SARS-CoV-2 in a panel
401 of laboratory cell lines, permissivity, and differences in growth profile. *Eur J Clin Microbiol*
402 *Infect Dis.* 2021; 40: 477–484.
- 403 30. Chu H, Chan JF, Yuen TT, Shuai H, Yuan S, Wang Y, Hu B, Yip CC, Tsang JO, Huang X,
404 Chai Y, Yang D, Hou Y, Chik KK, Zhang X, Fung AY, Tsoi HW, Cai JP, Chan WM, Ip JD, Chu
405 AW, Zhou J, Lung DC, Kok KH, To KK, Tsang OT, Chan KH, Yuen KY. Comparative tropism,
406 replication kinetics, and cell damage profiling of SARS-CoV-2 and SARS-CoV with
407 implications for clinical manifestations, transmissibility, and laboratory studies of COVID-
408 19: an observational study. *Lancet Microbe* 2020; 1(1): e14–e23.
- 409 31. Matsuyama S, Ujike M, Morikawa S, Tashiro M, Taguchi F. Protease-mediated
410 enhancement of severe acute respiratory syndrome coronavirus infection. *Proc Natl Acad*
411 *Sci U S A* 2005; 102: 12543–12547.
- 412 32. Osada N, Kohara A, Yamaji T, Hirayama N, Kasai F, Sekizuka T, Kuroda M, Hanada K.
413 The genome landscape of the african green monkey kidney-derived vero cell line. *DNA*
414 *Res* 2014; 21: 673–683.
- 415 33. Bartkova J, Rezaei N, Liontos M, Karakaidos P, Kletsas D, Issaeva N, Vassiliou LV,
416 Kolettas E, Niforou K, Zoumpourlis VC, Takaoka M, Nakagawa H, Tort F, Fugger K,
417 Johansson F, Sehested M, Andersen CL, Dyrskjot L, Ørntoft T, Lukas J, Kittas C, Helleday T,
418 Halazonetis TD, Bartek J, Gorgoulis VG. Oncogene-induced senescence is part of the
419 tumorigenesis barrier imposed by DNA damage checkpoints. *Nature* 2006; 444: 633–637.
- 420 34. Gorgoulis VG, Pefani DE, Pateras IS, Trougakos IP. Integrating the DNA damage and
421 protein stress responses during cancer development and treatment. *J Pathol* 2018; 246:
422 12-40.

- 423 35. Herranz N, Gil J. Mechanisms and functions of cellular senescence. *J Clin Invest*
424 2018; 128: 1238–1246.
- 425 36. Zamaraev AV, Zhivotovsky B, Kopeina GS. Viral Infections: Negative Regulators of
426 Apoptosis and Oncogenic Factors. *Biochemistry (Mosc)* 2020; 85: 1191–1201.
- 427 37. Li S, Zhang Y, Guan Z, Li H, Ye M, Chen X, Shen J, Zhou Y, Shi ZL, Zhou P, Peng K.
428 SARS-CoV-2 triggers inflammatory responses and cell death through caspase-8 activation.
429 *Signal Transduct Target Ther* 2020; 5: 235.
- 430 38. Ren Y, Shu T, Wu D, Mu J, Wang C, Huang M, Han Y, Zhang XY, Zhou W, Qiu Y, Zhou
431 X. The ORF3a protein of SARS-CoV-2 induces apoptosis in cells. *Cell Mol Immunol* 2020;
432 17: 881–883.
- 433 39. Venkatesan S, Angelova M, Puttick C, Zhai H, Caswell DR, Lu WT, Dietzen M,
434 Galanos P, Evangelou K, Bellelli R, Lim EL, Watkins TBK, Rowan A, Teixeira VH, Zhao Y,
435 Chen H, Ngo B, Zalmas LP, Al Bakir M, Hobor S, Gronroos E, Pennycuick A, Nigro E,
436 Campbell BB, Brown WL, Akarca AU, Marafioti T, Wu MY, Howell M, Boulton SJ, Bertoli C,
437 Fenton TR, de Bruin RAM, Maya-Mendoza A, Santoni-Rugiu E, Hynds RE, Gorgoulis VG,
438 Jamal-Hanjani M, McGranahan N, Harris RS, Janes SM, Bartkova J, Bakhoun SF, Bartek J,
439 Kanu N, Swanton C, Consortium T. Induction of APOBEC3 exacerbates DNA replication
440 stress and chromosomal instability in early breast and lung cancer evolution. *Cancer*
441 *Discov* 2021; candisc.0725.2020.
- 442 40. Chemudupati M, Kenney AD, Bonifati S, Zani A, McMichael TM, Wu L, Yount JS.
443 From APOBEC to ZAP: Diverse mechanisms used by cellular restriction factors to inhibit
444 virus infections. *Biochim Biophys Acta Mol Cell Res.* 2019; 1866: 382-394.

- 445 41. Malavolta M, Giacconi R, Brunetti D, Provinciali M, Maggi F. Exploring the Relevance
446 of Senotherapeutics for the Current SARS-CoV-2 Emergency and Similar Future Global
447 Health Threats. *Cells* 2020; 9: 909.
- 448 42. Hickson LJ, Langhi Prata LGP, Bobart SA, Evans TK, Giorgadze N, Hashmi SK, Herrmann
449 SM, Jensen MD, Jia Q, Jordan KL, Kellogg TA, Khosla S, Koerber DM, Lagnado AB, Lawson
450 DK, LeBrasseur NK, Lerman LO, McDonald KM, McKenzie TJ, Passos JF, Pignolo RJ,
451 Pirtskhalava T, Saadiq IM, Schaefer KK, Textor SC, Victorelli SG, Volkman TL, Xue A,
452 Wentworth MA, Wissler Gerdes EO, Zhu Y, Tchkonja T, Kirkland JL. Senolytics decrease
453 senescent cells in humans: Preliminary report from a clinical trial of Dasatinib plus
454 Quercetin in individuals with diabetic kidney disease. *EBioMedicine* 2019; 47: 446-456.
- 455 43. Kirkland JL, Tchkonja T. Senolytic drugs: from discovery to translation. *J Intern Med*
456 2020; 288: 518–536.
- 457

458 **Figure Legends**

459

460 **Figure 1: Detection of SARS-CoV-2 in lung cells. A.** Representative images of SARS-CoV-2
461 IHC staining in COVID-19 lung tissue. Competition with anti-peptide (S protein) showing
462 specificity of the IHC staining. Representative negative, control IHC staining in non-
463 COVID-19 lung tissues. Graph shows quantification of SARS-CoV-2 staining in the clinical
464 samples (**Suppl Table 1**). **B.** Detection of SARS-CoV-2 in AT2 cells (confirmed by TTF-1
465 staining) and in ACE-2 expressing cells. Double IHC staining for SARS-CoV-2 and TTF-1. **C.**
466 Detection of SARS-CoV-2 by transmission electron microscopy (TEM) in a representative
467 COVID-19 patient. Presence of SARS-CoV-2 within AT2 cells (**i,ii**) and of virions in the
468 proximity of the endoplasmic reticulum (**iii,iv**) as well as in cytoplasmic vesicles (**iii,v-vi**).
469 Corresponding scale bars are depicted. ICH: immunohistochemistry; AT2: alveolar type 2
470 cells; ACE2: angiotensin-converting enzyme 2, ***Statistical significant: $p < 0.001$.

471

472 **Figure 2: Senescence in SARS-CoV-2 infected cells. A.** Representative images of SARS-
473 CoV-2, SenTraGor (senescence) and ACE-2 staining in serial sections of COVID-19 lung
474 tissue. Double-immunostaining analysis (**2**) for SARS-CoV-2, SenTraGor (senescence),
475 ACE-2 and p16^{INK4A} in COVID-19 lung tissue. **B.** Representative results from serial staining
476 for SARS-CoV-2, SenTraGor (senescence) and ACE-2, and double-staining experiment for
477 SARS-CoV-2 and p16^{INK4A} in non-COVID-19 lung tissue. **C.** Graphs depicting the increased
478 levels of SenTraGor and p16^{INK4A} in COVID-19 lung tissue. Corresponding scale bars are
479 depicted. Statistical significance: **: $p < 0.01$; ***: $p < 0.001$.

480

481 **Figure 3. SARS-CoV-2 infection, senescence and SASP expression in Vero cells. A.** SARS-
482 CoV-2 presence (1), senescence induction (2), cellular proliferation (3) and DNA damage
483 activation (4), with corresponding quantitative histograms, in Vero cells with and without
484 SARS-CoV-2 infection. Double IHC staining for SARS-CoV-2 infection/senescence
485 induction (5) and senescence induction/cellular proliferation (6). **B.** Graph depicting
486 induction of SASP related cytokines following SARS-CoV-2 infection (mRNA expression).
487 **Statistical significant: $p < 0.01$.

488

489 **Figure 4: Senescence associated secretory phenotype (SASP) in COVID-19 lung tissues.**
490 **A.** Representative staining results (at low and high magnification) of SenTraGor, IL-6, IL-
491 1β and TTF-1 in corresponding serial sections (1) and as double immunostaining analysis
492 (2) of COVID-19 lung tissue. Original magnification: 400x. **B.** Representative staining
493 results showing absence or minimal levels of SenTraGor, IL-6 and IL- 1β in age-matched
494 non-COVID-19 control samples. Corresponding scale bars are depicted. IL-1 β : Interleukin
495 1β ; IL-6: Interleukin-6; ***Statistical significant: $p < 0.0001$.

496

497 **Supplementary Information**

498 **Suppl Figure legends**

499

500 **Suppl Figure 1: SARS-CoV-2 antibody production and screening selection. A.** Workflow
501 of the procedure for antibody production. **B.** Sequel of screening steps for antibody
502 production and selection. **C.** Final screening step processes leading to the selection of G2
503 monoclonal antibody (**Suppl Figure 2**).

504

505 **Suppl Figure 2:** Graph depicting the structure of G2 antibody as well as the DNA
506 sequences of FRs and CDRs elements of variable regions.

507

508 **Suppl Figure 3:** Graph depicting abundance of APOBEC 3G and 3H expression levels in
509 Vero cells by RT-qPCR analysis. *Statistical significant: $p < 0.05$.

510

511 **Suppl Figure 4:** APOBEC consensus RNA 2D sequence and structure motifs. **A.** Mutation
512 profile of SARS-CoV-2 genome exhibits APOBEC mutation signatures. Applying
513 bioinformatics analysis, C to U mutations were found to be the most dominant (55%),
514 suggesting an APOBEC driven signature. 56.8% of these mutations were confirmed to
515 exert APOBEC binding characteristics. **B.** Depicts the APOBEC consensus 2D structure
516 image as obtained from Beam software with statistics for the motif as shown in **(C)** and
517 the position of the motif on the 120 nt window as presented in **(D)**. APOBEC average
518 probability per base of being unpaired around a 120 nt region of the most probable C→U
519 site. **E.** The average probability from all C→U sites as obtained from the RNAplfold

520 algorithm is depicted **(i)** while **(ii)** presents the consensus sequence motif relative to the
521 average probability window.

522

523 **Suppl Figure 5: Infected senescent cells as a putative source for SARS-CoV-2 quasi-**

524 **species generation. A. (i)** Schematic layout presenting representative APOBEC sites from

525 the GISAID database analysis that overlap with the C→U sites of Vero cells after 17 days

526 of infection with the SARS-CoV-2 B.1.222 strain (see also panel **B**). The yellow bars show

527 the frequency of C→U substitutions when observing the GISAID database read counts

528 (green pileups) and with red is the C→U frequency when observing the SARS-CoV-2

529 genome, 17 days post infection. These representative sites are ranked as highest

530 relatively to the C→U counts as observed from the GISAID database. The genomic co-

531 ordinates of each C→U can be observed at the superimposed SARS-CoV-2 genome. On

532 the left of the graphs is the consensus motif when performing a motif analysis of all the

533 C→U sites of the SARS-CoV-2 genome, 17 days post infection. NGS reads were confirmed

534 in triplicate reads. **(ii)** Graph depicting frequency of nucleotide substitutions that

535 accumulated in the genome of B.1.222 strain following 17 days of infection. **(iii)** Pie chart

536 demonstrating that predominant C→U substitutions (65%) are APOBEC driven. **B.**

537 Additional locations of C→U substitutions observed in the genome of the SARS-CoV-2

538 progeny after 17 days of infection in Vero cells (relative to panel **A**).

539

540 **Material and Methods**

541

542 **RNA extraction and Reverse-Transcription real-time PCR (RT-qPCR) detection**

543 ***SASP cytokine and APOBEC G and H mRNA analysis***

544 RNA was extracted using the Nucleospin RNA kit (Macherey-Nagel #740955) according to
545 the manufacturer's instructions. 1 µg RNA was used for cDNA preparation with
546 Primescript™ RT Reagent Kit (Takara #RR037A). RT-qPCR was performed utilizing SYBR
547 Select Master Mix (Life technologies #4472908) on a DNA-Engine-Opticon (MJ-Research)
548 thermal cycler. Primer sequences employed were: *IL-1β* Fw: 5'-
549 GGAAGACAAATTGCATGG-3', Rv: 5'-CCCAACTGGTACATCAGCAC-3'; *IL-6* Fw: 5'-
550 AGAGGCACTGGCAGAAAAC-3', Rv: 5'-TGCAGGAACTGGATCAGGAC-3'; *IL-8* Fw: 5'-
551 AGGACAAGAGCCAGGAAGAA-3', Rv: 5'-ACTGCACCTTCACACAGAGC-3'; *APOBEC3G* Fw: 5'-
552 CCGAGGACCCGAAGGTTAC-3', Rv: 5'- TCCAACAGTGCTGAAATTCG-3'; *APOBEC3H* Fw: 5'-
553 CGACGGCTTGAAAGGATAGAG-3', Rv: 5'- TGAGTTGTGTGTTGACGATGA-3'; B2M: β2-
554 microglobulin (reference) gene Fw: 5'-TCTCTGGCTGGATTGGTATCT-3', Rv: 5'-
555 CAGAATAGGCTGCTGTTCTATC-3' (1). Results, averaged from three independent
556 experiments, are presented as n-fold changes after Sars-CoV-2 infection relatively to the
557 non-infected condition, using the 2-ΔΔCT method.

558

559 ***Viral RNA detection***

560 RNA was extracted using the NucleoSpin Virus RNA purification kit (Macherey-Nagel
561 #740.983) according to the manufacturer's instructions. RT-qPCR was performed utilizing
562 the One Step PrimeScript III RT-PCR Kit (Takara # RR601B) on a Rotor-Gene Q 6000

563 (Qiagen) thermal cycler following the manufacturer's instructions and using the CDC N-
564 gene directed primers [[https://www.cdc.gov/coronavirus/2019-ncov/lab/rt-pcr-panel-
565 primer-probes.html](https://www.cdc.gov/coronavirus/2019-ncov/lab/rt-pcr-panel-primer-probes.html)].

566

567 **Anti-SARS-COV-2 antibodies**

568 ***Generation***

569 A series of monoclonal antibodies against SARS-CoV2 spike protein were produced
570 according to a modified method of Koehler and Milstein (Koehler and Milstein,
571 1975). Briefly, twelve BALB/c mice of 5 weeks of age were immunized intraperitoneally
572 (i.p.) with 25µg of SARS-Cov2 protein (Trenzyme GmbH, Germany). All immunization and
573 animal handling were in accordance with animal care guidelines as specified in EU
574 Directive 2010/63/EU. After 5 cycles of immunization, mice were sacrificed, spleenocytes
575 were collected and fused with P3X63Ag8.653 (ATCC® CRL1580™) following a modified
576 method of Koehler and Milstein. Positive clones and antibody specificity were
577 determined through extensive immunosorbent assays. Four clones, namely 479-S1, 480-
578 S2, 481-S3 and 482-S4 are under patent application (**Gorgoulis V.G., Vassilakos D. and
579 Kastrinakis N. (2020) GR patent application no: 22-0003846810**).

580

581 ***RNA sequence determination and amino acid prediction***

582 RNA was collected from biological duplicates of generated hybridomas as described
583 elsewhere (2). RNA samples were processed according to manufacturer's instructions,
584 using the following kits: NEBNext® Poly(A) mRNA Magnetic Isolation Module (E7490S),
585 NEBNext® Multiplex Oligos for Illumina® (Index Primers Set 1, NEB7335) and

586 NEBNext® Ultra™ II Directional RNA Library Prep with Sample Purification Beads
587 (E7765S). After successful QC (RNA 6000 Nano bioanalyzer, Agilent) and quantity
588 measurements (Qubit™ RNA HS Assay Kit, Thermofisher), 1ug was used for mRNA
589 selection, cDNA construction, adaptor ligation and PCR amplification (11 cycles),
590 according to the manufacturer's protocol:
591 ([https://international.neb.com/products/e7760-nebnext-ultra-ii-directional-rna-library-](https://international.neb.com/products/e7760-nebnext-ultra-ii-directional-rna-library-prep-kit-for-illumina#Product%20Information)
592 [prep-kit-for-illumina#Product%20Information](https://international.neb.com/products/e7760-nebnext-ultra-ii-directional-rna-library-prep-kit-for-illumina#Product%20Information)). The 479-G2-ATCACG index from NEB
593 E7335 was used. The final libraries were analyzed with Agilent High Sensitivity DNA Kit on
594 an Agilent bioanalyzer, quantitated (Qubit dsDNA HS Assay Kit, Thermofisher) and, after
595 multiplexing, were run using a NextSeq 500/550 Mid Output Kit v2.5 (150 cycles), paired
596 end mode on a NextSeq550 (Illumina) at final concentration 1,3pM with 1% PhiX Control
597 v3.
598 Fastq files were demultiplexed with Flexbar (3). Quality control of the Fastq files was
599 assessed with FastQC tools (4). Adapter sequences were removed with Cutadapt program
600 (5) with the following parameters: quality trimming was set to 20 and the minimum
601 allowed nucleotide length after trimming was 20 nucleotides using --pair-filter=any to
602 apply the filters to both paired reads. A two way alignment mode was followed to
603 identify the antibody clone. More precisely alignments were performed with Bowtie2 (6)
604 with parameters set as following: -D 20 -R 3 -N 1 -L 20 -i S,1,0.50 --no-mixed --no-
605 discordant against an index made from IMGT database <http://www.imgt.org/> having
606 downloaded all mouse and human IG genes. Also this mode of alignments was executed
607 for quality control and visualization of the aligned reads spanning the IG gene segments
608 on the genome browser. The second mode refers to the determination and

609 reconstruction of the clones. This was performed with MiXCR suite (7). At first,
610 alignments against the IG repertoire were performed with kaligner and visualization of
611 alignments was assessed. It was observed that the use of kaligner gave better results
612 with higher clone hits regarding the VH and VL segments. Full assembly of the clones was
613 performed. A full report of the number of reads and assembly of CDR and FR clones is
614 provided in clones479_S1kalign.txt. The clones with the highest number of reads and
615 coverage across the V,D,J segments were considered. The reported matched sequences
616 were also checked with IgBlast tool <https://www.ncbi.nlm.nih.gov/igblast/>. In addition,
617 after the assembly of the amino acid reconstruction of the FR and CDR regions of the full
618 variable fragment for both the Heavy and Light antibody chains, a 3D visualization was
619 also determined via folding the V protein fragment with iTasser suite (8). The above
620 analysis has been extensively described in **Gorgoulis VG, Vassilakos D and Kastrinakis N.**
621 **(2020) GR patent application no: 22-0003846810.**

622

623 **Immunocytochemistry (ICC)-Immunohistochemistry (IHC)**

624 Method: ICC and IHC were performed according to previous published protocols (9). In
625 brief, 3 µm thick sections from formalin-fixed paraffin embedded (FFPE) lung tissues were
626 employed. Antigen retrieval was heat-mediated in 10 mM citric acid (pH 6.0) for 15
627 minutes. The following primary antibodies were applied: i) the anti-SARS-CoV-2 (G2)
628 monoclonal antibody (dilution 1:300), ii) anti-ACE-2 [Rabbit polyclonal antibody Abcam,
629 Cat.no: ab15348 (dilution 1:200)], iii) anti- TTF-1 [rat monoclonal antibody Dako, Clone
630 8G7G3/1, Cat.no: M3575 (Ready-to-Use)], iv) anti-CD68 [mouse monoclonal antibody
631 Dako, Clone PG-M1, Cat.no: M0876 (dilution 1:50)] and v) anti-p16^{INK4A} [mouse

632 monoclonal antibody Santa Cruz, clone: F-12, Cat.no.:sc-1661. (dilution 1:100)], vi) IL-1 β
633 [Rabbit polyclonal antibody Abcam, Cat.no: ab2105 (dilution 1:150)] and vii) IL-6 [mouse
634 monoclonal antibody R&D systems, clone: Clone: 6708, Cat.no:MAB206 (dilution 1:100)],
635 all overnight at 4°C. Development of the signal was achieved using the Novolink Polymer
636 Detection System (Cat.no: RE7150-K, Leica Biosystems). Specimens were counterstained
637 with hematoxylin.

638 Negative Controls for the anti-SARS-CoV-2 (G2) monoclonal antibody: *i) Biological*,
639 comprising previously published and new lung tissue samples from a cohort of 50 cases
640 that underwent surgery prior to COVID-19 outbreak. *ii) Technical*: a. Omission of the G2
641 primary monoclonal antibody, b. Blocking of the G2 primary monoclonal antibody using
642 the corresponding S-protein (Cat.no.P2020-029, Trenzyme) in a 1:10 (G2/Spike protein)
643 ratio and c. Two slides per case were employed for each staining or control experiment.

644 Evaluation of G2 staining: Cells were considered positive irrespective of the staining
645 intensity. Two different semi-quantitative IHC evaluation approaches, previously
646 described were adopted (10,11) According to the first, the number of G2 positive cells
647 per 4mm² was encountered and scored according to the following criteria: (+) for positive
648 staining in <5 cells per 4 mm², (+) for positive staining in 5–50 cells per 4mm² and (+++)
649 for positive staining in >50 cells per 4 mm² (10). Regarding the second one, the number
650 of G2 positive cells per whole slide was estimated and subsequent scores were assessed:
651 (+) between one and five positive cells per whole slide (scattered cells), (++) more than
652 five cells per whole slide but no foci (isolated cells) and (+++) more than 10 cells in one \times
653 20 field (with foci) (11). For IL-6 and IL-1 β , the percentage of immunopositive cells was

654 encountered (12). Evaluations were performed blindly by four experienced pathologists
655 (KE, PF, CK and VG) and intra-observer variability was minimal ($p \leq 0.05$).

656

657 **Bioinformatic analysis for identification of mutational signatures in the SARS-CoV-2**
658 **genome**

659 ***Screening for mutational signatures in the SARS-CoV-2 genome***

660 To investigate the mutational properties on the SARS-CoV-2 genome we downloaded from
661 GISAID database (<https://www.gisaid.org/>) 423.000 available strains that were
662 distributed globally. These strains were aligned with the Wuhan first assembly
663 NC_045512, obtained from NCBI (<https://www.ncbi.nlm.nih.gov/sars-cov-2/>), with
664 Bowtie aligner (13) using the following command:

```
665 /bowtie2-2.4.2-sra-linux-x86_64/bowtie2-align-s --wrapper basic-0 -x Covncbiref -p 4 -D  
666 20 -R 3 - N 1 -L 20 -i S,1,0.50 -f allCov19.fa
```

667 In order to identify the mutations we have created an “in-house” script using *calmd*
668 function from SAMtools (14) , based on the analysis of deciphering mutations from the
669 proteome occupancy profile study (15). We applied the following commands for minus
670 and reverse stranded reads:

```
671 samtools sort accepted_hits.bam -o accepted_hitsort.bam
```

```
672 samtools rmdup -s accepted_hitsort.bam rmdupsorted.bam
```

```
673 #forward library
```

```
674 samtools view -h -f 0x0010 rmdupsorted.bam | samtools calmd -S -
```

```
675 ~/Desktop/Bioinformatics/NCBI.fa /dev/stdin |
```

```
676 /media/covid_meth/deademinatation_covid19/get_edit_stat.pl      '-'      >
677 Mapping_editStatus.bed
678 samtools view -h -F 0x0010 rmdupsorted.bam | samtools calmd -S -
679 ~/Desktop/Bioinformatics/NCBI.fa /dev/stdin |
680 /media/covid_meth/deademinatation_covid19/get_edit_stat.pl      '+'      >>
681 Mapping_editStatus.bed
682 #reverse library
683 samtools view -h -F 0x0010 rmdupsorted.bam | samtools calmd -S -
684 ~/Desktop/Bioinformatics/GRCh37/hg19.fa /dev/stdin |
685 /media//covid_meth/deademinatation_covid19/get_edit_stat.pl    '-'      >
686 Mapping_editStatus2.bed
687 samtools view -h -f 0x0010 rmdupsorted.bam | samtools calmd -S -
688 ~/Desktop/Bioinformatics/GRCh37/hg19.fa /dev/stdin |
689 /media//covid_meth/deademinatation_covid19/get_edit_stat.pl    '+'      >>
690 Mapping_editStatus2.bed
691 The scripts bellow were used in order to determine the counts per type of mutation and
692 filter for C→U or G→A mutations in respect with the strand orientation of the alignments.
693 Bedtools (16) have also been used to obtain the fasta sequences and the windows around
694 the C→U sites.
695 #sort reads
696 sort -k1,1 -k2,2n -k3,3nMapping_editStatus2.bed| uniq -c >
697 Mapp_editstat_APOBECcounts.bed sort -k1,1 -k2,2n -k3,3nMapping_editStatus2.bed|
```

698 `uniq -c > Mapp_editstat_APOBECcounts.bed sed -i 's/^ *//g'`

699 `Mapp_editstat_APOBECcounts.bed`

700 `#obtain the fasta`

701 `fastaFromBed -s -fi ~/Desktop/Bioinformatics/GRCh37/hg19.fa -`

702 `bedMapp_editstat_APOBECcounts.bed -tab -foAPOBEC_counts1fa.bed`

703 `#get mutation type C→U or A→G`

704 `perl fixmutstat.pl APOBEC_counts1fa.bed APOBEC_counts1facorrect`

705 Based on the filtered candidate sites with a frequency of mutations above than 5 reads

706 we have obtained windows of ± 60 nucleotides and folded the RNA sequences from these

707 regions with Vienna RNA fold algorithm (17) to determine the RNA 2D structure. SHAPE

708 reactivities from SHAPE-seq data (18) were used to guide the RNA folding.

709 `RNAfold --noPS --shape=forViennatest.SHAPE.txt --shapeConversion=S -g <`

710 `forViennatest..fa`

711 `>> test.txt.`

712 To decipher the candidate motifs we counted the frequency of letters ± 5 nucleotides

713 from the most frequent deademinated nucleotide. The frequency for each letter was

714 determined via a perl script which extracts all possible *k-mers* and their frequencies. Next

715 these *k-mers*, based on their frequency, were plotted with Web-logo motifs (19). In

716 addition position-weight matrices (PWM) for each letter around the deademinated RNA

717 nucleotide were extracted.

718 Our analysis on motifs and RNA structure for choosing the candidate APOBEC sites based

719 on publicly available known studies (20-22) that also demonstrate similar characteristics

720 regarding the motif specific APOBEC signature and RNA structure. From our analysis we

721 determined a CCT/A enrichment around regions of open hairpin structures agreeing with
722 the results from the literature.

723

724 ***Verification of APOBEC specific motifs by applying machine learning***

725 To filter and obtain scores for each APOBEC specific candidate site we have also applied a
726 machine learning scheme using convolutional neural networks having as input the
727 sequence and RNA structure around the candidate strongest APOBEC sites with high
728 frequency that also demonstrate a high potential for APOBEC binding.

729

730 ***APOBEC consensus RNA 2D sequence and structure motifs***

731 To determine the consensus RNA structure properties we have used the Vienna RNA
732 folding output dot bracket notation, which performed the folding based on the icSHAPE
733 reactivities as input to BEAM program (23). In addition, the binding sites from (19) have
734 been used to decipher the structure for the hg19. The structure properties for the
735 APOBEC sites on the hg19 have been folded using SHAPE (24) and DMS (25) data to guide
736 the RNA folding. Secondary RNA structure motifs regarding the hg19 have been
737 determined using BEAM software. Beam software was used as follows:

738 First the dot bracket notation is translated in a 24 letter language for structure called
739 Bear:

```
740 java -jar encoder.jar APOBEC.db APOBEC.fb
```

```
741 java -jar /$basepath3/BEAM_release_1.5.1.jar -f APOBEC.fb -w 15 -W 30 -M 5
```

742 Next, then consensus motifs are extracted, using as maximum threshold to output the
743 top 5 motifs with maximum width of motif set to 30 nucleotides.

744

745 **APOBEC average probability per base of being unpaired around a 120 nt region of the**
746 **most probable C→U site**

747 Furthermore RNAplfold has been used to extract the probabilities per base of being
748 unpaired having the following parameters

749 *RNAplfold -W 30 -L 15 -u 1 --shape=forViennatest.SHAPE.txt --shapeMethod=D --*
750 *shapeConversion=O -g <forViennatest..fa >> test.txt*

751 The output per sequence is a *_lunp* file where from these files the smoothed geometric
752 mean per base pair is extracted and plotted having the candidate deaminated site,
753 located in the center of the 120 nucleotide window. The plots are done in R using fit and
754 polygon functions from the standard R bioconductor packages. The confidence intervals
755 per base are calculated as $CI = \bar{x} \pm z \frac{s}{\sqrt{n}}$ where $z = 0.95$ % confidence, s =standard deviation
756 and n are the number of sequences ~ 3500 .

757 In order to accomplish docking of the APOBEC with the RNA substrates we have used
758 SimRNA suite (26) to determine the RNA 3D structure properties of the SARS-CoV-2 RNA
759 around the candidate C→U sites. DARS-RNP potential (27) has been used using PDB files
760 from crystallographic data for APOBEC3G with PDB code 6bux and 6k3j (28) from the PDB
761 database (<https://www.rcsb.org/>) for docking the RNAs as obtained from SimRNA with
762 APOBEC. Scores were ranked and the RNAs with docking scores higher than 1 standard
763 deviation over the mean were used for the extraction of consensus motifs both in terms
764 of structure and sequence. Regarding the sequence motif a window of ± 10 nt around the
765 high docking score was obtained and according to the *k-mer* distribution PWM matrices
766 are extracted and plotted with web-logo.

767 The SimRNA commands to extract the 3D RNA structure are the following:

768 ./SimRNA -s 3D_testVf.fa -c config2.dat -S 3D_test.struct -o tRNAs python2

769 trafl_extract_lowestE_frame.py tRNAs.trafl"

770 ./SimRNA_trafl2pdb tRNAs-000001.pdb tRNAs_minE.trafl : AA" perl configpdb2.pl

771 tRNAs_minE-000001_AA.pdb tRNAs.config"

772 The configuration file for the 3D simulations is set as:

773 *NUMBER_OF_ITERATIONS 160000*

774 *TRA_WRITE_IN_EVERY_N_ITERATIONS 16000*

775 *INIT_TEMP 1.35*

776 *FINAL_TEMP 0.90*

777 *BONDS_WEIGHT 1.0*

778 *ANGLES_WEIGHT 1.0*

779 *TORS_ANGLES_WEIGHT 0.0*

780 *ETA_THETA_WEIGHT 0.40*

781 *SECOND_STRC_RESTRAINTS_WEIGHT 1.0*

782 *FRACTION_OF_NITROGEN_ATOM_MOVES 0.10*

783 *FRACTION_OF_ONE_ATOM_MOVES 0.45*

784 *FRACTION_OF_TWO_ATOMS_MOVES 0.44*

785 *FRACTION_OF_FRAGMENT_MOVES 0.01*

786 In order to visualize the properties that might determine the binding of APOBEC, the

787 power of integrated gradients tools (29) were used to obtain the motifs. Our analysis is

788 based upon an already developed method DeepRipe (30) adding an extra module to also

789 incorporate the RNA structure information. The classifier has been trained to distinguish

790 such motifs which are characteristic for APOBEC binding.

791

792 **Supplementary References**

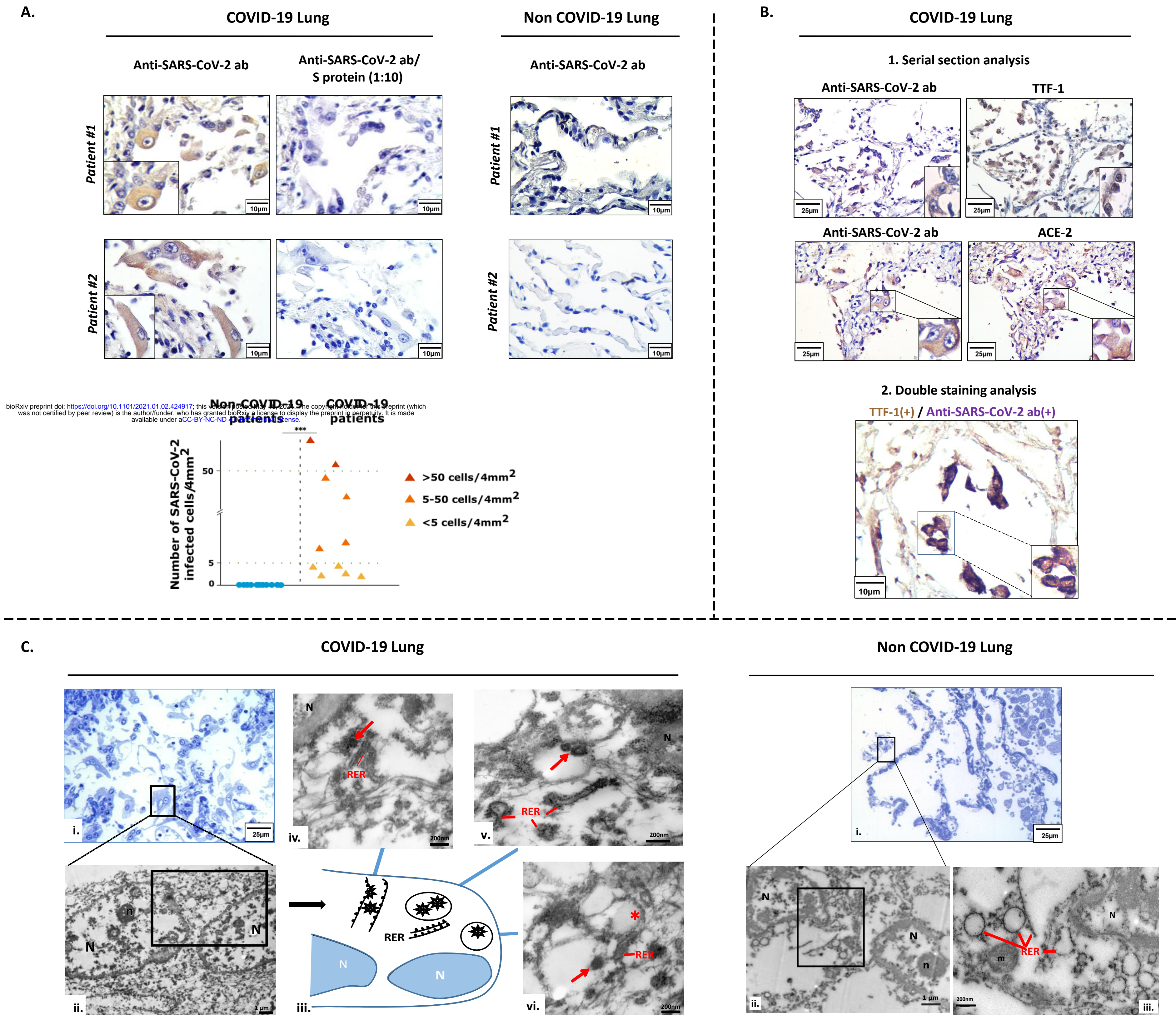
- 793 1. Huan CC, Wang HX, Sheng XX, Wang R, Wang X, Liao Y, Liu QF, Tong GZ, Ding C, Fan
794 HJ, Wu JQ, Mao X. Porcine epidemic diarrhea virus nucleoprotein contributes to HMGB1
795 transcription and release by interacting with C/EBP- β . *Oncotarget* 2016; 7; 75064–75080.
- 796 2. Komseli ES, Pateras IS, Krejsgaard T, Stawiski K, Rizou SV, Polyzos A, Roumelioti FM,
797 Chiourea M, Mourkioti I, Paparouna E, Zampetidi s CP, Gumeni S, Trougakos IP, Pefani
798 DE, O'Neill E, Gagos S, Eliopoulos AG, Fendler W, Chowdhury D, Bartek J, Gorgoulis VG. A
799 prototypical non-malignant epithelial model to study genome dynamics and concurrently
800 monitor micro-RNAs and proteins in situ during oncogene-induced senescence. *BMC*
801 *Genomics* 2018; 19: 37.
- 802 3. Dodt M, Roehr JT, Ahmed R, Dieterich C. FLEXBAR-Flexible Barcode and Adapter
803 Processing for Next-Generation Sequencing Platforms. *Biology (Basel)* 2012; 1: 895–905.
- 804 4. Andrew SA. quality control tool for high throughput sequence data. *Fast QC* 2010;
805 532.
- 806 5. Martin M. Cutadapt removes adapter sequences from high-throughput sequencing
807 reads. *EMBnet J* 2011; 17: 10-12.
- 808 6. Langmead B, Salzberg SL. Fast gapped-read alignment with Bowtie 2. *Nat Methods*
809 2012; 9: 357-359.
- 810 7. Bolotin DA, Poslavsky S, Davydov AN, Frenkel FE, Fanchi L, Zolotareva OI, Hemmers
811 S, Putintseva EV, Obratzsova AS, Shugay M, Ataulakhanov RI, Rudensky AY, Schumacher
812 TN, Chudakov DM. Antigen receptor repertoire profiling from RNA-seq data. *Nat*
813 *Biotechnol* 2017; 35: 908–911.

- 814 8. Yang J, Yan R, Roy A, Xu D, Poisson J, Zhang Y. The I-TASSER Suite: protein structure
815 and function prediction. *Nature Methods* 2015; 12: 7–8.
- 816 9. Evangelou K, Lougiakis N, Rizou SV, Kotsinas A, Kletsas D, Muñoz-Espín D,
817 Kastrinakis NG, Pouli N, Marakos P, Townsend P, Serrano M, Bartek J, Gorgoulis VG.
818 Robust, universal biomarker assay to detect senescent cells in biological specimens.
819 *Aging Cell* 2017; 16: 192–197.
- 820 10. Schaefer IM, Padera RF, Solomon IH, Kanjilal S, Hammer MM, Hornick JL, Sholl LM.
821 In situ detection of SARS-CoV-2 in lungs and airways of patients with COVID-19. *Mod*
822 *Pathol* 2020; 33: 2104–2114.
- 823 11. Rimmelink M, De Mendonça R, D'Haene N, De Clercq S, Verocq C, Lebrun L, Lavis P,
824 Racu ML, Trépant AL, Maris C, Rorive S, Goffard JC, De Witte O, Peluso L, Vincent JL,
825 Decaestecker C, Taccone FS, Salmon I. Unspecific post-mortem findings despite
826 multiorgan viral spread in COVID-19 patients. *Crit Care* 2020; 24: 495.
- 827 12. van Vliet T, Varela-Eirin M, Wang B, Borghesan M, Brandenburg SM, Franzin R,
828 Evangelou K, Seelen M, Gorgoulis V, Demaria M. Physiological hypoxia restrains the
829 senescence-associated secretory phenotype via AMPK-mediated mTOR suppression. *Mol*
830 *Cell* 2021; S1097-2765(21)00213-6.
- 831 13. Langmead B, Trapnell C, Pop M, Salzberg SL. Ultrafast and memory-efficient
832 alignment of short DNA sequences to the human genome. *Genome Biol* 2009; 10: R25.
- 833 14. Li H, Handsaker B, Wysoker A, Fennell T, Ruan J, Homer N, Marth G, Abecasis G,
834 Durbin R; 1000 Genome Project Data Processing Subgroup. The Sequence
835 Alignment/Map format and SAMtools. *Bioinformatics* 2009; 25: 2078–2079.

- 836 15. Schueler M, Munschauer M, Gregersen LH, Finzel A, Loewer A, Chen W, Landthaler
837 M, Dieterich C. Differential protein occupancy profiling of the mRNA transcriptome.
838 *Genome Biol* 2014; 15: R15.
- 839 16. Quinlan AR, Hall IM. BEDTools: a flexible suite of utilities for comparing genomic
840 features. *Bioinformatics* 2010; 26: 841–842.
- 841 17. Gruber AR, Lorenz R, Bernhart SH, Neuböck R, Hofacker IL. The Vienna RNA
842 websuite. *Nucleic Acids Res* 2008; 36(Web Server issue): W70–W74.
- 843 18. Manfredonia I, Nithin C, Ponce-Salvatierra A, Ghosh P, Wirecki TK, Marinus T,
844 Ogando NS, Snijder EJ, van Hemert MJ, Bujnicki JM, Incarnato D. Genome-wide mapping
845 of SARS-CoV-2 RNA structures identifies therapeutically-relevant elements. *Nucleic Acids*
846 *Res* 2020; 48: 12436–12452.
- 847 19. Crooks GE, Hon G, Chandonia JM, Brenner SE. WebLogo: a sequence logo
848 generator. *Genome Res* 2004; 14: 1188–1190.
- 849 20. Sharma S, Patnaik SK, Taggart RT, Baysal BE. The double-domain cytidine
850 deaminase APOBEC3G is a cellular site-specific RNA editing enzyme. *Sci Rep* 2016; 6:
851 39100.
- 852 21. Sharma S, Baysal BE. Stem-loop structure preference for site-specific RNA editing
853 by APOBEC3A and APOBEC3G. *PeerJ* 2017; 5: e4136.
- 854 22. York A, Kutluay SB, Errando M, Bieniasz PD. The RNA Binding Specificity of Human
855 APOBEC3 Proteins Resembles That of HIV-1 Nucleocapsid. *PLoS Pathog* 2016; 12:
856 e1005833.

- 857 23. Pietrosanto M, Mattei E, Helmer-Citterich M, Ferrè F. A novel method for the
858 identification of conserved structural patterns in RNA: From small scale to high-
859 throughput applications. *Nucleic Acids Res* 2016; 44: 8600–8609.
- 860 24. Spitale RC, Flynn RA, Zhang QC, Crisalli P, Lee B, Jung JW, Kuchelmeister HY, Batista
861 PJ, Torre EA, Kool ET, Chang HY. Erratum: Structural imprints in vivo decode RNA
862 regulatory mechanisms. *Nature* 2015; 527: 264.
- 863 25. Rouskin S, Zubradt M, Washietl S, Kellis M, Weissman JS. Genome-wide probing of
864 RNA structure reveals active unfolding of mRNA structures in vivo. *Nature* 2014; 505:
865 701–705.
- 866 26. Boniecki MJ, Lach G, Dawson WK, Tomala K, Lukasz P, Soltysinski T, Rother KM,
867 Bujnicki JM. SimRNA: a coarse-grained method for RNA folding simulations and 3D
868 structure prediction. *Nucleic Acids Res* 2016; 44: e63.
- 869 27. Tuszynska I, Bujnicki JM. DARS-RNP and QUASI-RNP: new statistical potentials for
870 protein-RNA docking. *BMC Bioinformatics* 2011; 12: 348.
- 871 28. Maiti A, Myint W, Kanai T, Delviks-Frankenberry K, Sierra Rodriguez C, Pathak VK,
872 Schiffer CA, Matsuo H. Crystal structure of the catalytic domain of HIV-1 restriction factor
873 APOBEC3G in complex with ssDNA. *Nat Commun* 2018; 9: 2460.
- 874 29. Sundararajan, Mukund, Ankur Taly, and Qiqi Yan. "Axiomatic attribution for deep
875 networks." In *International Conference on Machine Learning*, pp. 3319-3328. PMLR,
876 2017.
- 877 30. Ghanbari M, Ohler U. Deep neural networks for interpreting RNA-binding protein
878 target preferences. *Genome Res* 2020; 30: 214–226.

FIGURE 1



bioRxiv preprint doi: <https://doi.org/10.1101/2021.01.02.424917>; this version posted January 2, 2021. The copyright holder for this preprint (which was not certified by peer review) is the author/funder, who has granted bioRxiv a license to display the preprint in perpetuity. It is made available under aCC-BY-NC-ND 4.0 International license.

FIGURE 2.

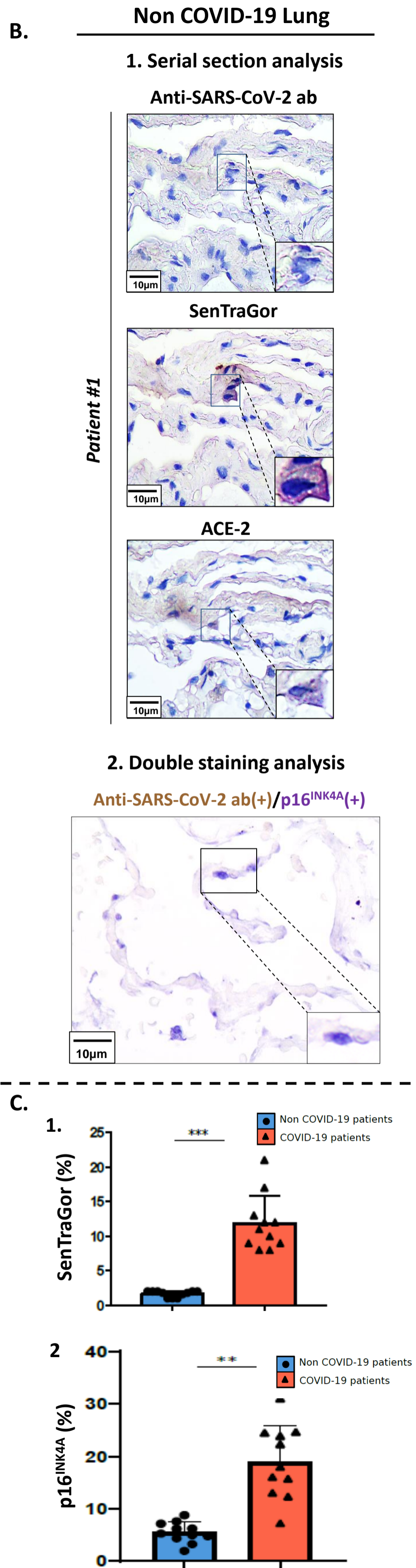
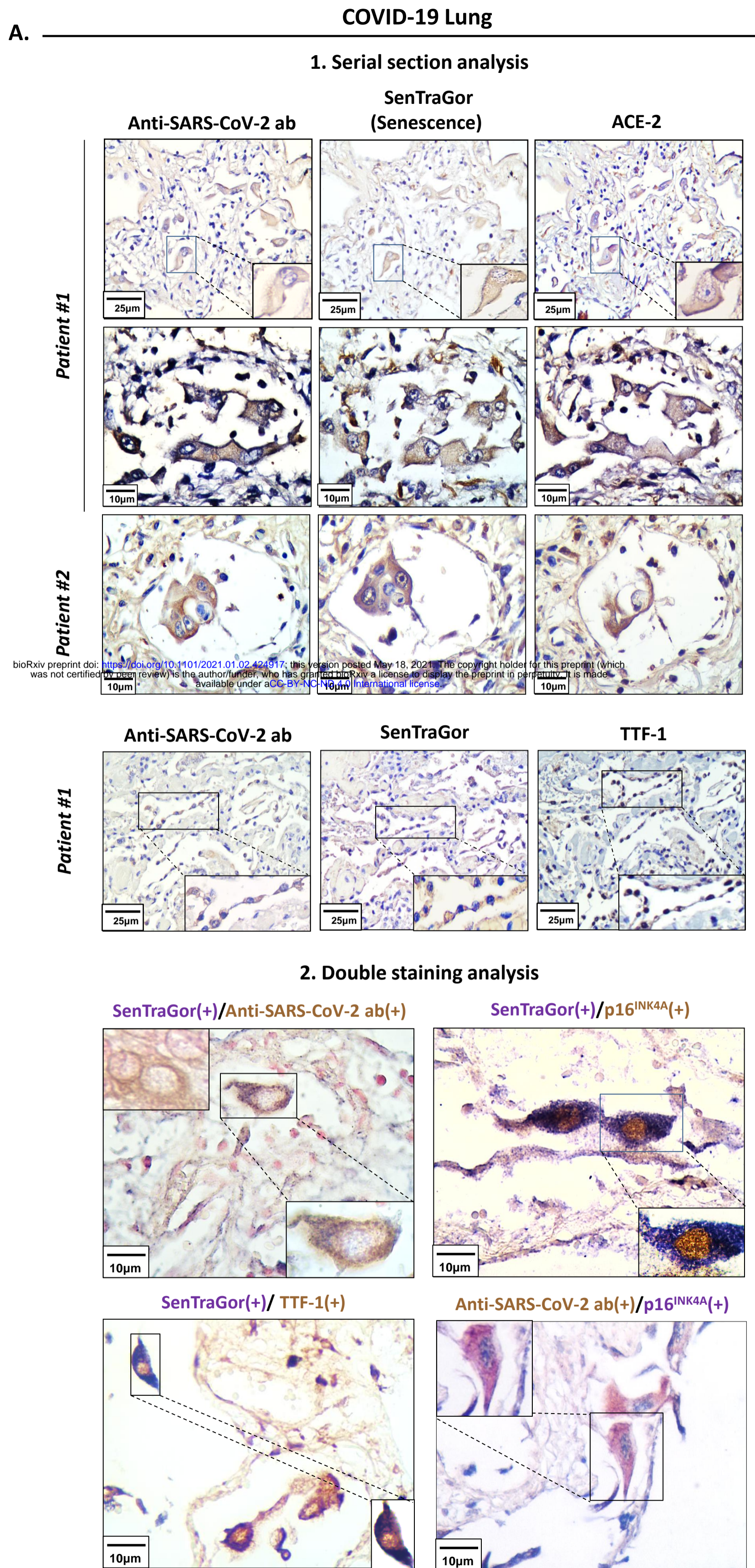


Figure 3

Vero cells

bioRxiv preprint doi: <https://doi.org/10.1101/2021.01.02.424917>; this version posted May 18, 2021. The copyright holder for this preprint (which was not certified by peer review) is the author/funder, who has granted bioRxiv a license to display the preprint in perpetuity. It is made available under aCC-BY-NC-ND 4.0 International license.

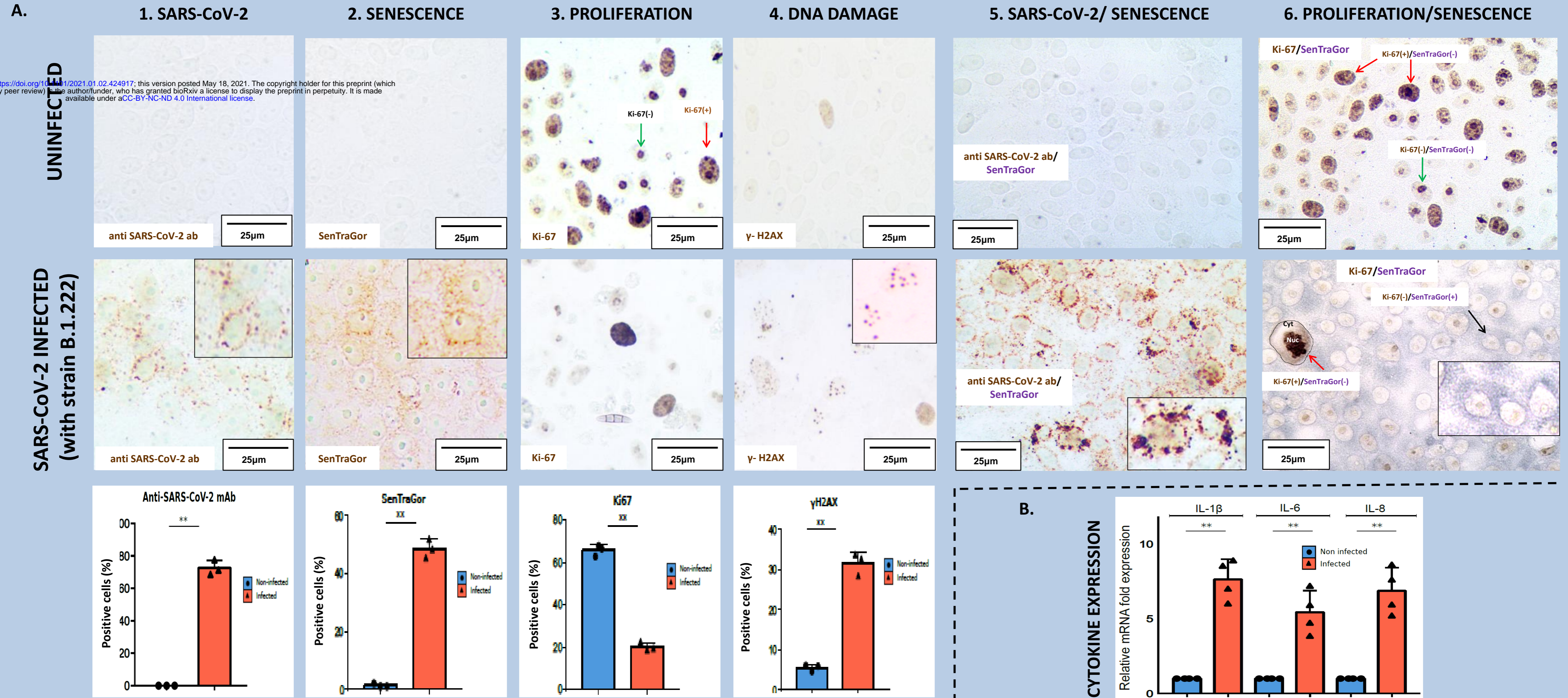
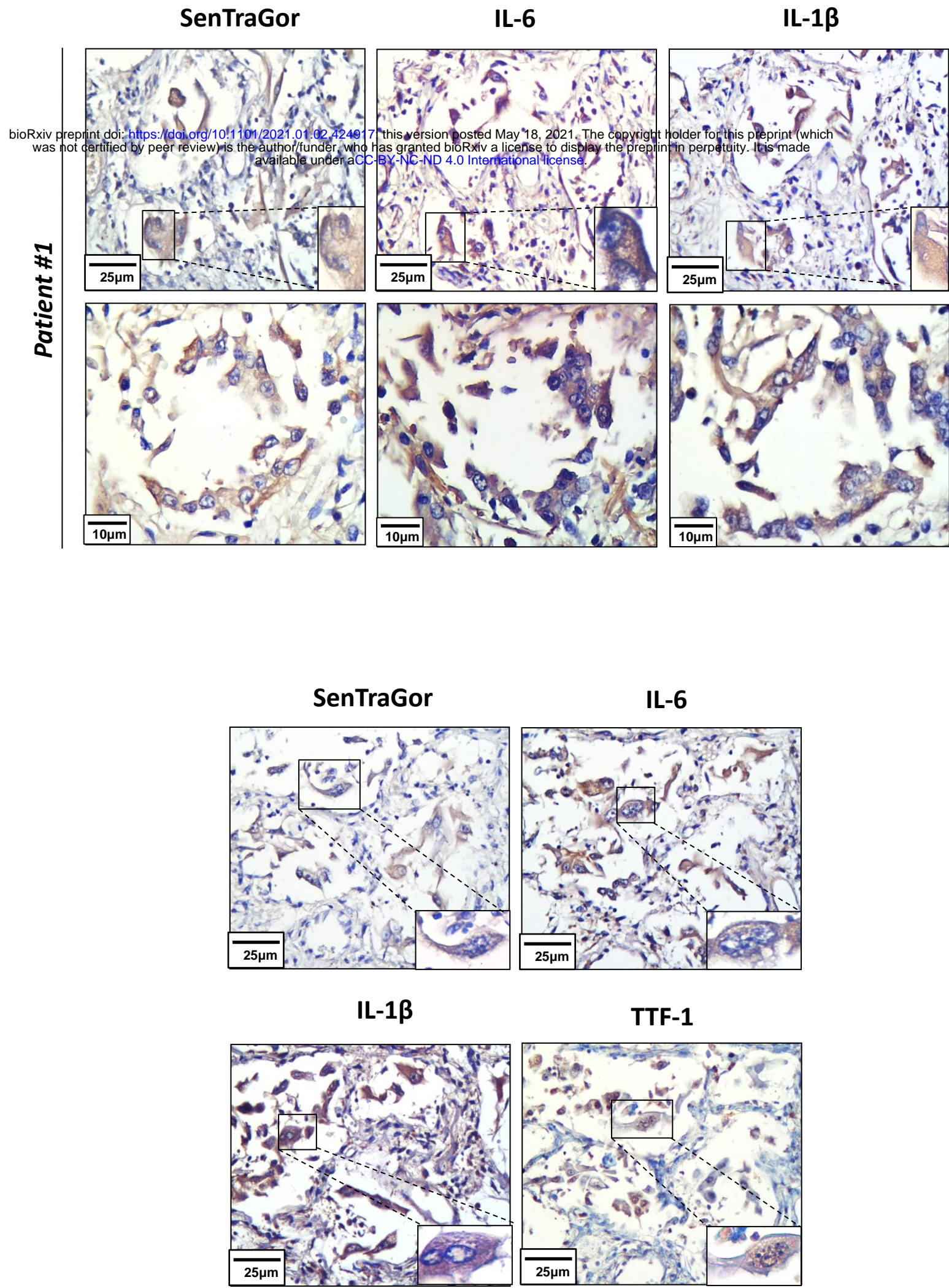


FIGURE 4.

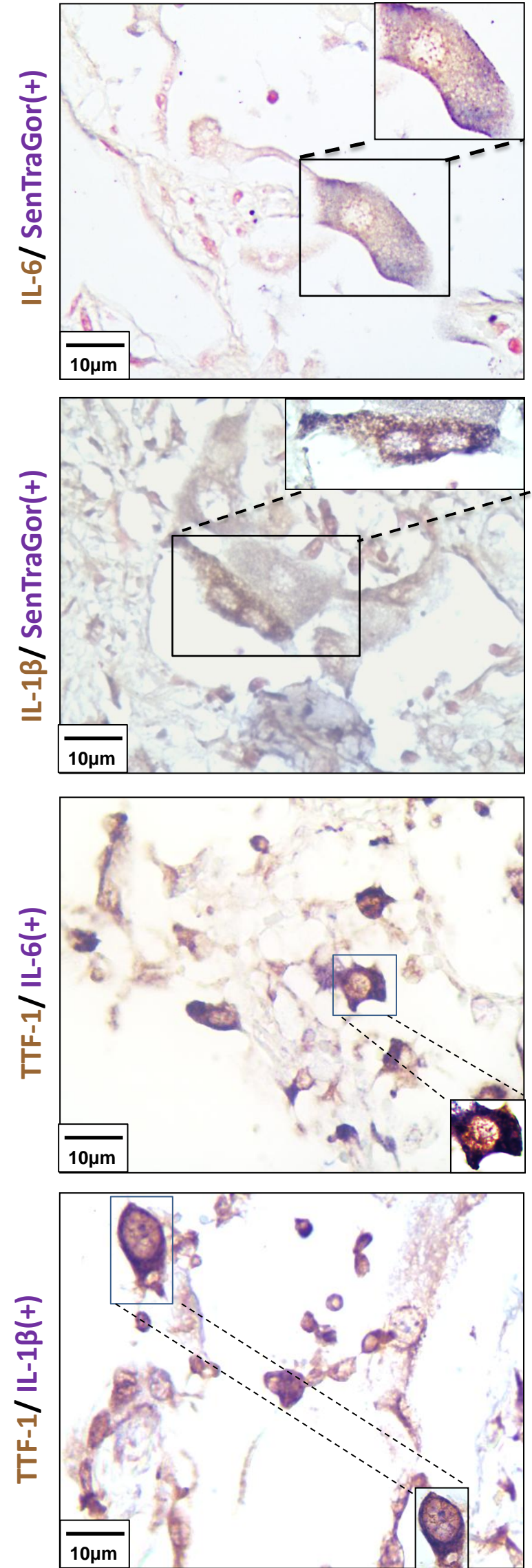
COVID-19 Lung

A.

1. Serial section analysis



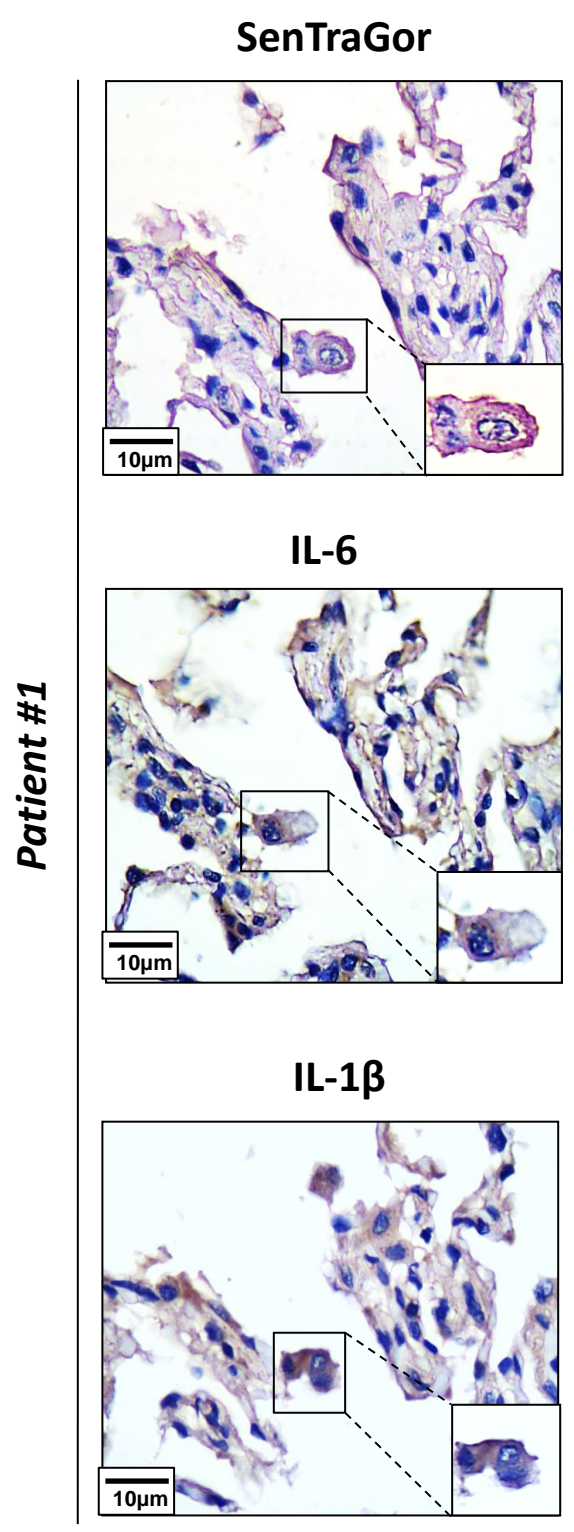
2. Double staining analysis



Non COVID-19 Lung

B.

Serial section analysis



C.

